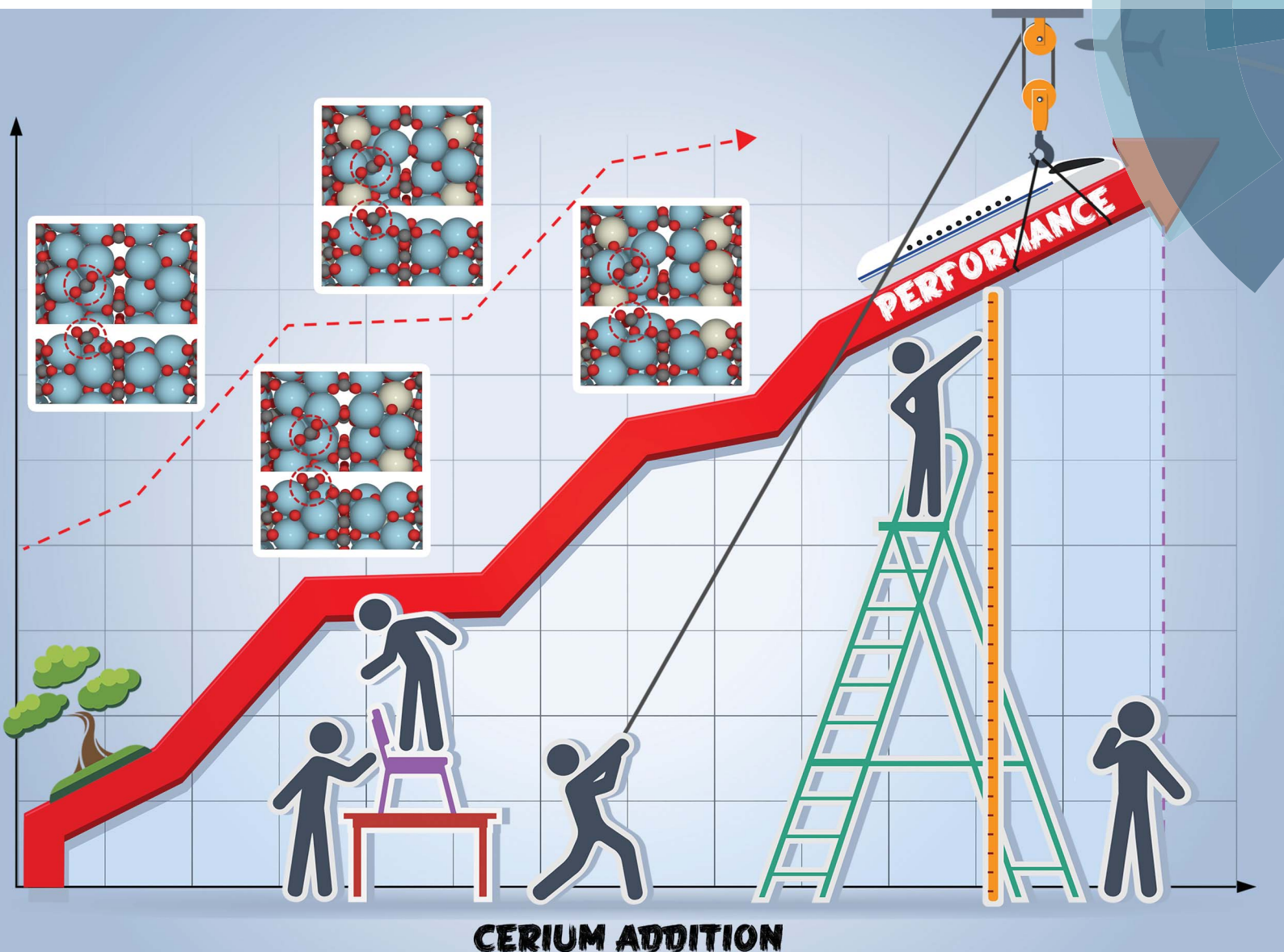


Chemical Science

rsc.li/chemical-science



CERIUM ADDITION

ISSN 2041-6539



ROYAL SOCIETY
OF CHEMISTRY

EDGE ARTICLE

Jinlong Gong *et al.*

On the role of Ce in CO₂ adsorption and activation
over lanthanum species

Cite this: *Chem. Sci.*, 2018, 9, 3426On the role of Ce in CO₂ adsorption and activation over lanthanum species†Xinyu Li,^{‡ab} Zhi-Jian Zhao,^{‡ab} Liang Zeng,^{ab} Jiubing Zhao,^{ab} Hao Tian,^{ab} Sai Chen,^{ab} Kang Li,^{ab} Sier Sang^{ab} and Jinlong Gong^{id}*^{ab}

La₂O₃ exhibits good performance for various catalytic applications, such as oxidative coupling of methane (OCM) and dry reforming of methane (DRM), during which coke formation may lead to the deactivation of catalysts. Typically, the reaction between CO₂ adsorbed on La₂O₃ and coke is the rate-determining step of the coke elimination process. This paper describes the influence of Ce addition on the CO₂ adsorption and activation over La₂O₃. Combined with *in situ* and *ex situ* characterization and density functional theory (DFT) calculation, we show that Ce addition promotes the formation of bidentate carbonate on La₂O₃ via tuning CO₂ adsorption energy. In addition, Ce addition adjusts the ratio of bidentate/monodentate carbonate, and affects the ratio of hexagonal/monoclinic La₂O₂CO₃ on the binary oxides. DRM is used as a probe reaction to examine the coke elimination performance of Ce–La binary oxide. It is found that when the Ce/La ratio reaches the optimal value (0.15), Ce–La binary oxide has the highest CO₂ adsorption energy and predominantly promotes the formation of bidentate carbonate, and hence possesses the highest basicity above 700 °C and finally exhibits the best coke elimination performance.

Received 13th January 2018
Accepted 23rd February 2018

DOI: 10.1039/c8sc00203g

rsc.li/chemical-science

Introduction

La₂O₃, as a common rare earth oxide with strong basicity, is generally used as a support or promotor to facilitate CO₂ adsorption and activation.^{1–4} Typically, CO₂ adsorbs on the surface of La₂O₃ and subsequently converts La₂O₃ to La₂O₂CO₃.^{5,6} The formed La₂O₂CO₃ species actively reacts with coke thus enhancing catalyst stability.^{5–8} Additionally, La₂O₂CO₃ plays a significant role in the oxidative coupling of methane (OCM), and CH₄ can be activated over the surface of La₂O₂CO₃.^{9,10} La₂O₂CO₃ has three phases including tetragonal (I type), monoclinic (Ia type), and hexagonal (II type).^{11,12} As treatment temperature increases, phase transformation happens. Transformation from I-La₂O₂CO₃ to Ia-La₂O₂CO₃ takes place readily, namely Ia-La₂O₂CO₃ is the monoclinic distortion of I-La₂O₂CO₃.^{12,13} Conversion of Ia-La₂O₂CO₃ to II-La₂O₂CO₃ is a slow process below 600 °C.¹² And II-La₂O₂CO₃ decomposes to La₂O₃ at about 750 °C.¹⁴ It has been reported that the orientation of carbonate ions is closely related to the crystalline phase of La₂O₂CO₃,^{11,15} both of which can affect the catalytic performance.^{16,17} It has been found that mixing ZnO

with La₂O₂CO₃ increases the basicity of the La₂O₂CO₃ material.¹⁸ In addition, Metiu *et al.* reported that dopants can affect CH₄ activation and dissociation on lanthanum oxide and hence improve the OCM performance.^{19,20}

Generally, ceria possesses good redox properties and has various applications.^{21,22} It has been extensively used as an oxygen carrier²³ and is a necessary component of catalysts used in reforming processes,^{24–26} water–gas shift reaction,²⁷ CO oxidation,²⁸ and soot combustion.^{29,30} In order to improve the oxygen storage capacity (OSC) and oxygen mobility (OM) of ceria, an appropriate dopant is typically mixed with ceria to enhance the OSC/OM of ceria.^{31–33} La³⁺, as an aliovalent dopant, has been extensively applied to enhance the OSC/OM of ceria,^{34–36} during which oxygen vacancies can be formed due to the charge compensation mechanism.^{37,38} It should be noted that the reported synergy of Ce–La binary oxide is based on the fact that La addition can largely promote the formation of oxygen vacancy on ceria,^{36–38} while this paper investigates the influence of Ce addition on the properties of lanthanum species.

Since the release or uptake of lattice oxygen is closely related to an oxygen/steam atmosphere, herein an oxygen/steam atmosphere is excluded to minimize the involvement of oxygen vacancy. Thus, CO₂ as a soft oxidant is selected due to its weak oxidation capacity compared with O₂ or H₂O molecule. Given that CO₂ adsorbs on the surface of La₂O₃ and reacts with La₂O₃ to form La₂O₂CO₃,^{5,6} the effect of Ce addition on the properties of La₂O₂CO₃ formed under the mild oxidative conditions has been investigated. For the OCM reaction, coke

*Key Laboratory for Green Chemical Technology of Ministry of Education, School of Chemical Engineering and Technology, Tianjin University, Tianjin 300072, China.
E-mail: jlgong@tju.edu.cn

^bCollaborative Innovation Center of Chemical Science and Engineering (Tianjin), Tianjin 300072, China

† Electronic supplementary information (ESI) available. See DOI: 10.1039/c8sc00203g

‡ These authors contributed equally to this work.

deposition is negligible in an oxidative atmosphere, but it takes place under oxygen lean conditions.^{39,40} When O₂ is replaced by CO₂ to rule out the influence of oxygen vacancy, dry reforming of methane (DRM) mainly occurs, during which CH₄ reacts with CO₂ to form syngas (CO and H₂). For the DRM reaction, coke deposition and sintering of metal particles can lead to the deactivation of catalysts.^{4,41} Herein, the DRM reaction is used as a probe reaction to examine the coke elimination performance of Ce–La binary oxides.

This paper demonstrates the influence of Ce addition on the properties of lanthanum species, including the adsorption mode of CO₂ (bidentate carbonate and monodentate carbonate) and the crystalline phase of lanthanum oxycarbonate (hexagonal La₂O₂CO₃ and monoclinic La₂O₂CO₃) formed after CO₂ and CH₄ adsorption. *In situ* diffuse reflectance infrared Fourier transform spectroscopy (DRIFTS) measurements are applied to investigate surface species on the Ce–La binary oxide during the process of CO₂/CH₄ adsorption. The physical–chemical properties of the catalysts prior to and after CO₂/CH₄ adsorption are investigated by X-ray diffraction (XRD), X-ray photoelectron spectroscopy (XPS), Raman spectra, N₂-physisorption, transmission electron microscopy (TEM), and H₂ temperature-programmed reduction (H₂-TPR). Periodic density functional theory (DFT) calculations are carried out to estimate CO₂ adsorption energy on Ce–La binary oxides. DRM is selected as the probe reaction to examine the performance of coke elimination, and CO₂ temperature-programmed desorption (CO₂-TPD) and thermogravimetric analysis (TGA) are applied to examine the basicity of Ce–La binary oxides and properties of the deposited coke during the DRM process.

Results and discussion

Textural properties of Ce–La binary oxide

Table 1 sums up the textural properties of the samples with different Ce/La ratios at the moment of “0 min” (Fig. 1, see details in the Experimental section). XRD patterns of a series of Ce–La binary oxides at “0 min” are shown in Fig. 2a and b. Hexagonal lanthanum oxycarbonate (II-La₂O₂CO₃, JCPDF#37-0804) acts as the dominant species for the series of Ce–La binary oxides. When the Ce/La ratio reaches 0.10 and higher, monoclinic lanthanum oxycarbonate (Ia-La₂O₂CO₃, JCPDF#48-1113) can be detected but is minimal. Results show that the

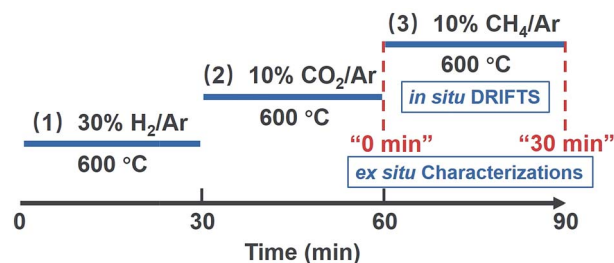


Fig. 1 Overview of the experimental method for *in situ* and *ex situ* reaction conditions during measurement.

peaks of La₂O₂CO₃ gradually migrate to a higher degree (Fig. 2b), indicating that lattice parameters decrease correspondingly (Table 1). Since the ionic radius of either Ce³⁺ (0.101 nm) or Ce⁴⁺ (0.097 nm) is smaller than that of La³⁺ (0.11 nm),³⁷ the decrease of lattice parameters could be attributed to the fact that Ce-ions are doped into the lattice of La₂O₂CO₃.⁴² Furthermore, the surface areas of the series of Ce–La binary oxides were obtained through the N₂ sorption isotherm method. With the increase of Ce/La ratios, surface area gradually decreases, which is related to the decrease of lanthanum composition in the binary oxide and the small surface area of the cerium composition. The types of carbonate, formed upon CO₂ adsorption, have a close relationship with the crystalline phases of La₂O₂CO₃, which will be discussed in the following part.

The valence state of cerium (Fig. 3) and the surface elemental composition (Table 1) were also examined. On the basis of literature reports,^{43–47} the Ce 3d region consists of five doublets. The spin–orbit components with unprimed labels, *v* and *u*, are ascribed to the primary Ce 3d_{5/2} and Ce 3d_{3/2} states while other doublets represent satellite features arising from the Ce 3d_{5/2} and Ce 3d_{3/2} ionization.^{44,46,48} The doublets labeled *v*₀/*u*₀ and *v*[′]/*u*[′] are characteristic of Ce³⁺, while the remaining doublets labeled *v*/*u*, *v*[″]/*u*[″] and *v*^{″″}/*u*^{″″} are characteristic of Ce⁴⁺.^{44,46} The Ce³⁺ surface concentration was calculated *via* the following equation:^{44,48}

$$c_{\text{Ce}^{3+}} = \frac{I(v_0) + I(v') + I(u_0) + I(u')}{\sum_i (I(u') + I(v'))} \quad (1)$$

where *c_x* denotes the concentration of *x* and *I*(*y*) denotes the integral intensity of the specific peak. It should be noted that

Table 1 Textural properties of the series of Ce–La binary oxide

Sample	Molar ratio of Ce/La		Lattice parameter ^c (Å)		Surface area ^d (m ² g ^{−1})	Average pore diameter ^d (nm)	Pore volume ^d (cm ³ g ^{−1})
	Bulk ^a	Surface ^b	<i>a</i>	<i>b</i>			
0Ce–LOC	0	0	4.078	15.950	47	28.4	0.22
0.05Ce–LOC	0.049	0.21	4.075	15.940	43	16.1	0.20
0.10Ce–LOC	0.102	0.18	4.074	15.933	33	14.4	0.14
0.15Ce–LOC	0.149	0.23	4.068	15.923	25	11.6	0.09
0.20Ce–LOC	0.203	0.22	4.065	15.854	14	10.0	0.08

^a Determined by ICP-OES. ^b Determined by XPS. ^c Determined by XRD patterns prior to CH₄ adsorption. ^d Determined by N₂-physisorption.



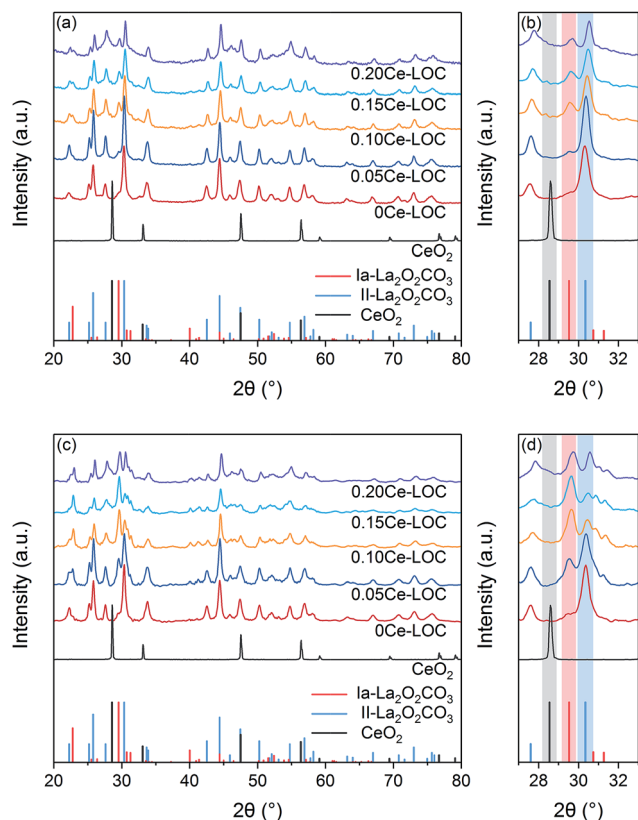


Fig. 2 XRD patterns of the series of Ce–La binary oxide prior to and after CH₄ adsorption for 30 min. (a) Full scale at “0 min”, (b) details with enlarged scale at “0 min”, (c) full scale at “30 min” and (d) details with enlarged scale at “30 min”. Color bars in (b) and (d) are auxiliary lines.

the Ce³⁺ content of CeO₂ is 21% while other Ce–La binary oxides have much higher Ce³⁺ content than CeO₂ (Fig. 3). It is assumed that the enhanced content of Ce³⁺ is doped into the lattice of La₂O₂CO₃ to maintain the concentration of Ce³⁺, which is consistent with the reduced lattice parameter. As the Ce/La ratio

increases from 0.05 to 0.20, the Ce³⁺ content gradually decreases (Fig. 3), indicating that the trend to be doped into the lattice of La₂O₂CO₃ is close to saturated state and Ce⁴⁺ might exist in the form of CeO₂ distributed on the surface of the binary oxide. Additionally, CeO₂ diffraction peaks are absent even in the enlarged graph of XRD patterns (Fig. 2b), which suggests that CeO₂ particles are uniformly dispersed on the surface of the Ce–La binary oxide. For the series of Ce–La binary oxides (Table 1), bulk Ce/La ratios obtained from ICP-OES were consistent with nominal Ce/La ratios, while surface Ce/La ratios obtained from XPS are higher than bulk Ce/La ratios. The difference in Ce/La ratios between the bulk and surface mainly results from the selected subsequent impregnation method, namely La₂O₂CO₃ was first synthesized and then impregnated with Ce precursor solution so that cerium mainly distributed on the surface of the binary oxide.

The morphology and structure of Ce–La binary oxides with different Ce/La ratios were characterized *via* TEM (Fig. S1 in the ESI†). Particles randomly distribute along the surface of La₂O₂CO₃, and some of them are confirmed as CeO₂. It can be found that small particles have continuous lattice fringes with the oxide hosts, indicating the formation of the solid solution on the interface between the observed small particles and oxide hosts.³⁷ Since CeO₂ diffraction peaks are absent in XRD patterns (Fig. 2), UV-vis is applied to measure the indirect band gap of CeO₂, which reflects variation tendency in the size of CeO₂ particles located on the surface of the samples.^{49,50} The indirect band gaps of non-oriented polycrystalline CeO₂ and La₂O₃ are 3.19 eV,⁴⁹ and 5.2 eV,⁵¹ respectively. As shown in Fig. S2 in the ESI†, the indirect band gap of CeO₂ migrates to a lower value with the increase of Ce/La ratios, indicating the corresponding increment in the size of CeO₂ particles on the surface of binary oxides. In addition, the variation tendency of the increment remains the same when the Ce/La ratio reaches 0.15 and 0.20. It is reported that the concentration of Ce³⁺ increases with the reduction in CeO₂ particle size.⁴⁷ Therefore, the obtained results of UV-vis (Fig. S2 in the ESI†) have a similar variation tendency with the results of XPS (Fig. 3).

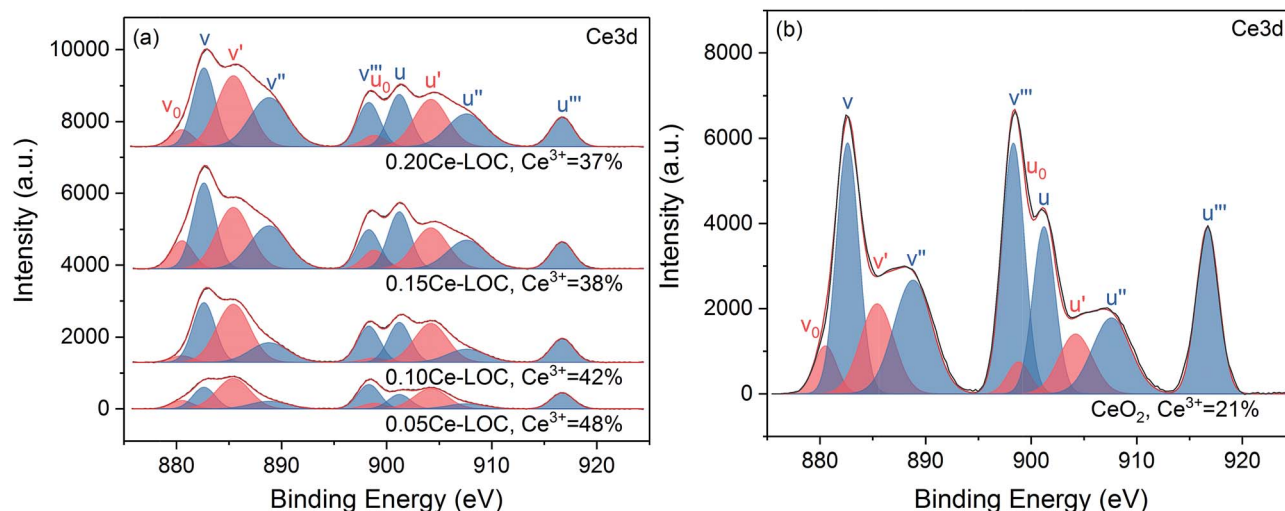


Fig. 3 Fitting of core-level Ce 3d XPS profiles of (a) the series of Ce–La binary oxide and (b) CeO₂.



In situ DRIFTS measurements

In situ DRIFTS measurements are applied in order to identify surface intermediates present on the Ce–La binary oxide samples from “0 min” to “30 min” (see the definition in the Experimental section), during which coke is formed *via* CH₄ decomposition and will further react with carbonate formed after CO₂ adsorption (Fig. 1). *In situ* DRIFTS spectra are shown in Fig. 4, and corresponding contour graphs are inserted in the *x*–*y* planes of Fig. 4 and listed alone in Fig. S3 in the ESI†. The band at 1300 cm^{−1} corresponds to the C–H bending of gaseous methane,^{24,52,53} and it can be found on all samples. The strong band at 1563 cm^{−1} corresponds to bidentate carbonate with the coexistence of bands at 1300, 1029 and 856 cm^{−1},^{15,54,55} while the strong band at 1345 cm^{−1} is ascribed to monodentate carbonate with the coexistence of bands at 1428, 1070 and 856 cm^{−1}.^{15,54,55} In addition, bands at 1748 and 1796 cm^{−1} are overtones of C=O stretching vibration and CO₃^{2−} stretching vibration.¹⁵

For the series of La–Ce binary oxides, both bidentate carbonate and monodentate carbonate exist on the surface (Fig. 4 and S3 in the ESI†), while for CeO₂, bidentate carbonate is absent (Fig. 4f and S3f in the ESI†). At “0 min”, the intensity of bidentate carbonate on La–Ce binary oxides increases as the Ce/La ratio increases from 0 to 0.15, reaches the maximum when the Ce/La ratio is 0.15, and finally decreases slightly when the Ce/La ratio reaches 0.20 (Fig. S3 and S4 in the ESI†).

Simultaneously, the intensity of monodentate carbonate shows a variation tendency, which is opposite to the intensity of bidentate carbonate. Therefore, it is assumed that Ce addition can influence the CO₂ adsorption mode on the surface of Ce–La binary oxide and promote the transformation from monodentate carbonate to bidentate carbonate.

When CO₂ is adsorbed on La₂O₃ (30 min prior to “0 min” in Fig. 1), it reacts with La₂O₃ and then leads to the formation of La₂O₂CO₃. During the *in situ* DRIFTS measurement (from “0 min” to “30 min” in Fig. 1), CH₄ can be adsorbed on the surfaces of La₂O₂CO₃ and dissociates to form coke under non-oxidative conditions,^{39,40} while coke will react with La₂O₂CO₃ to form La₂O₃ and CO.^{5,8} For the series of Ce–La binary oxides, the intensity of bidentate carbonate keeps decreasing as time on stream goes by, while the intensity of monodentate carbonate remains stable (Fig. 5 and S3 in the ESI†). Therefore, bidentate carbonate is consumed to react with coke during the introduction of CH₄. It is concluded that bidentate carbonate is active in the reaction with the coke, while monodentate carbonate is inactive (Fig. 4, S3 and S4 in the ESI†). If we use I_B/I_M (intensity of ~1563 cm^{−1}/intensity of ~1345 cm^{−1}) to evaluate the ratio of bidentate carbonate to monodentate carbonate, it is found that when the Ce/La ratio equals 0.15, Ce–La binary oxide possesses the highest ratio of I_B/I_M (Fig. 5). Considering that Ce addition can affect the ratio of I_B/I_M , it is

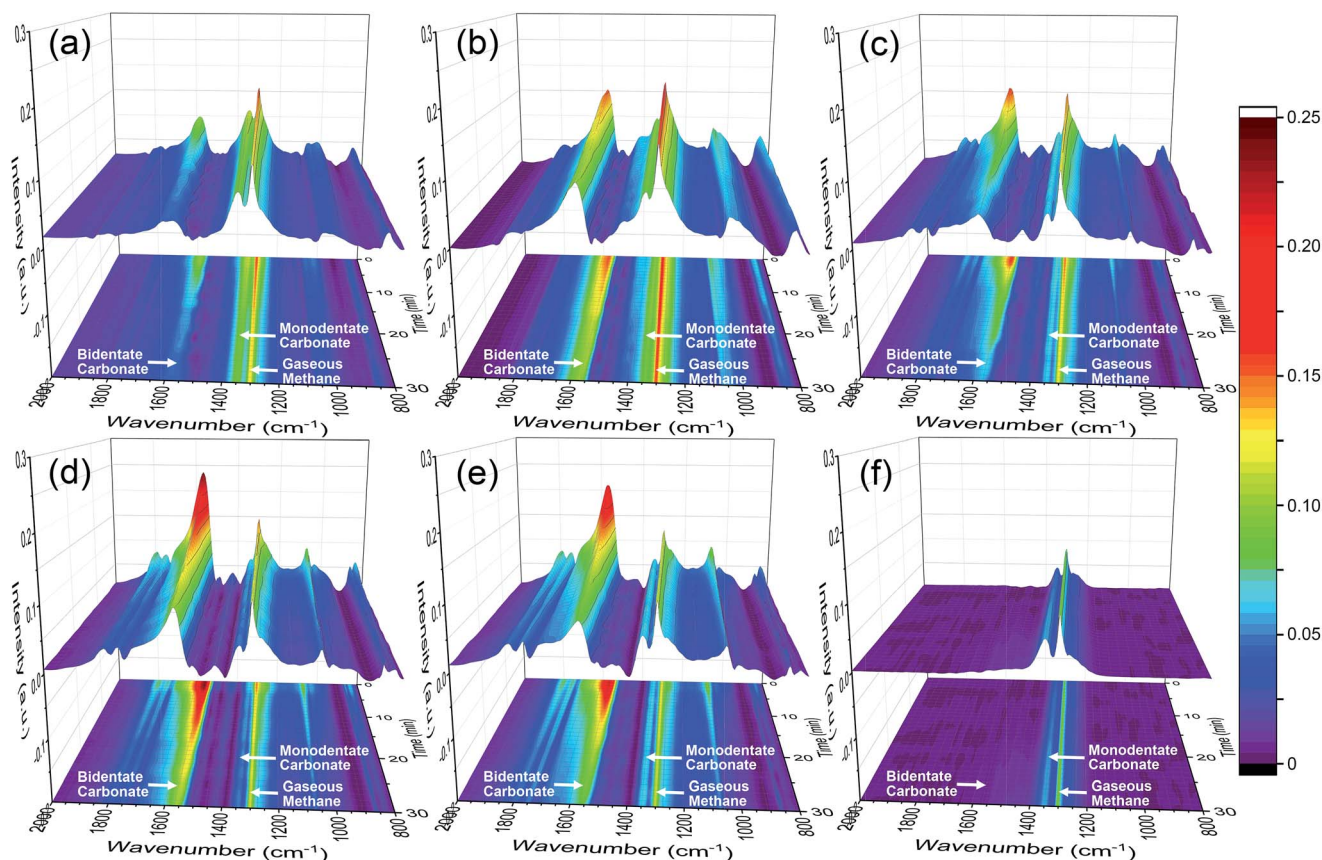


Fig. 4 DRIFTS spectra for the series of Ce–La binary oxide during CH₄ adsorption for 30 min. (a) 0Ce–LOC, (b) 0.05Ce–LOC, (c) 0.10Ce–LOC, (d) 0.15Ce–LOC, (e) 0.20Ce–LOC and (f) CeO₂.



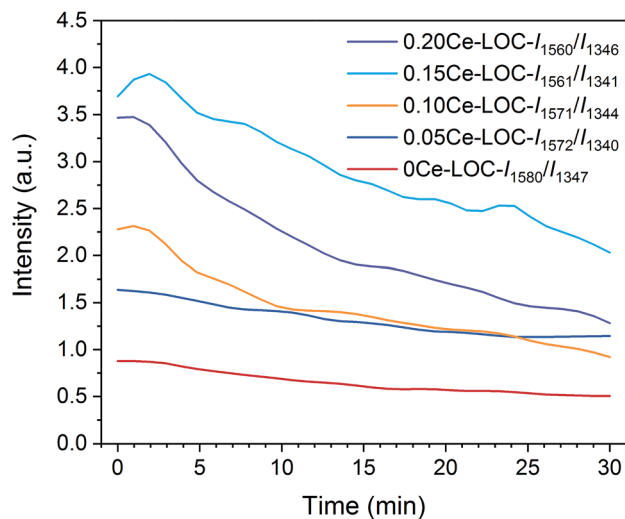


Fig. 5 The intensity ratios of bidentate/monodentate carbonate in DRIFTS spectra as a function of time on stream.

assumed that Ce addition might affect the performance of coke elimination, which will be discussed in the following part.

Influence on the crystalline phase

XRD patterns of the series of Ce–La binary oxides at “30 min” after reacting with CH_4 are shown in Fig. 2c and d. The CeO_2 phase remains absent indicating that cerium is well dispersed. By comparison of the XRD patterns of samples at “0 min” and “30 min”, the intensity of peaks ascribed to $\text{II-La}_2\text{O}_2\text{CO}_3$ decreases significantly compared with $\text{Ia-La}_2\text{O}_2\text{CO}_3$. In addition, it is observed that as the Ce/La ratio increases from 0 to 0.15, the decrease in the intensity of $\text{II-La}_2\text{O}_2\text{CO}_3$ peaks becomes much more prominent. The consumption of $\text{II-La}_2\text{O}_2\text{CO}_3$ during the CH_4 adsorption indicates that $\text{II-La}_2\text{O}_2\text{CO}_3$ is more active than $\text{Ia-La}_2\text{O}_2\text{CO}_3$ for coke elimination. For the 0.15Ce–LOC sample, the intensity of $\text{II-La}_2\text{O}_2\text{CO}_3$ is much lower than that of $\text{Ia-La}_2\text{O}_2\text{CO}_3$ so that $\text{Ia-La}_2\text{O}_2\text{CO}_3$ eventually becomes the dominant species on the sample, indicating that Ce addition can influence the decomposition of $\text{II-La}_2\text{O}_2\text{CO}_3$ caused by the reaction with deposited coke.

Raman spectra of samples at “30 min” are shown in Fig. 6, which are consistent with the XRD patterns. Peaks at 290, 333, 438, 451, 1052, and 1341 cm^{-1} correspond to $\text{Ia-La}_2\text{O}_2\text{CO}_3$, while peaks at 355, 385, 740, and 1082 cm^{-1} are assigned to $\text{II-La}_2\text{O}_2\text{CO}_3$.^{13,56,57} The intensity ratio of peaks at $355\text{ cm}^{-1}/451\text{ cm}^{-1}$ can be used as a descriptor to evaluate the dominant surface species. When the Ce/La ratios are 0 and 0.05, the $\text{II-La}_2\text{O}_2\text{CO}_3$ phase is the dominant surface species and $\text{Ia-La}_2\text{O}_2\text{CO}_3$ phase is the subordinate. However, when the Ce/La ratio is higher than 0.10, $\text{Ia-La}_2\text{O}_2\text{CO}_3$ acts as the dominant surface species. For 0.15Ce–LOC, it possesses the lowest intensity ratio of peaks at $355\text{ cm}^{-1}/451\text{ cm}^{-1}$, indicating that the ratio of $\text{II-La}_2\text{O}_2\text{CO}_3/\text{Ia-La}_2\text{O}_2\text{CO}_3$ reaches the lowest level. It can be assumed that $\text{II-La}_2\text{O}_2\text{CO}_3$ formed on the 0.15Ce–LOC sample has the fastest decomposition rate. Two additional

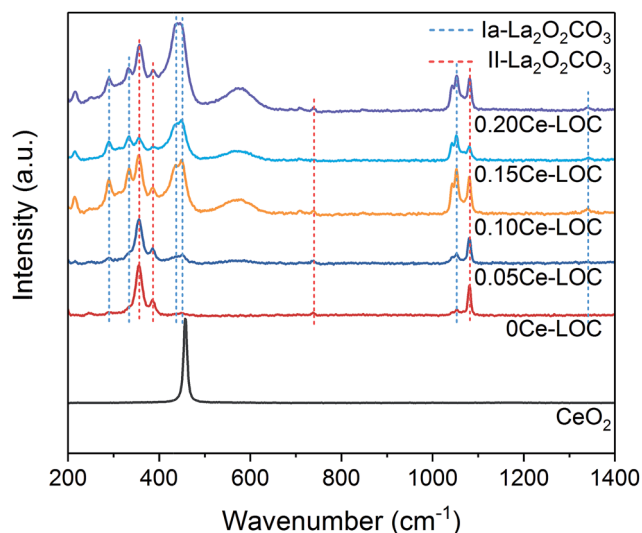


Fig. 6 Raman spectra of the series of Ce–La binary oxide upon CH_4 adsorption for 30 min.

peaks at 216 and 577 cm^{-1} are reported to be induced by the dopant,⁵⁸ which verifies the existence of Ce^{3+} in the lattices of the samples.^{59,60}

DRIFTS results demonstrate that Ce addition is capable of facilitating the formation of bidentate carbonate, which is active for coke elimination. Based on the XRD patterns (Fig. 2) and Raman spectra (Fig. 6), with the decomposition of bidentate carbonate, the ratio of $\text{II-La}_2\text{O}_2\text{CO}_3$ to $\text{Ia-La}_2\text{O}_2\text{CO}_3$ will change correspondingly. Spivey *et al.* directly ascribed FTIR bands at 1509 cm^{-1} and 1367 cm^{-1} to $\text{II-La}_2\text{O}_2\text{CO}_3$ and $\text{Ia-La}_2\text{O}_2\text{CO}_3$, respectively.¹⁶ They concluded that only $\text{II-La}_2\text{O}_2\text{CO}_3$ acts as a reactive species to eliminate coke while $\text{Ia-La}_2\text{O}_2\text{CO}_3$ merely acts as a spectator species.¹⁶ However, Kawi *et al.* reported that $\text{Ia-La}_2\text{O}_2\text{CO}_3$ mainly participated in coke elimination rather than $\text{II-La}_2\text{O}_2\text{CO}_3$.⁶¹ Combined with results of XRD patterns, Raman spectra and *in situ* DRIFTS spectra, we could conclude that bidentate carbonate is active for coke elimination and closely related to the $\text{II-La}_2\text{O}_2\text{CO}_3$ phase while monodentate carbonate is inactive for coke elimination and closely related to the $\text{Ia-La}_2\text{O}_2\text{CO}_3$ phase.

Catalytic performance of coke elimination

H_2 -TPR was carried out to investigate the decomposition behavior of $\text{La}_2\text{O}_2\text{CO}_3$ formed on the series of Ce–La binary oxide under a H_2 atmosphere. The H_2 -TPR profiles are shown in Fig. 7. It should be mentioned that the formation of a reduction peak in H_2 -TPR profiles is due to the reaction of H_2 and CO_2 released during the decomposition of $\text{La}_2\text{O}_2\text{CO}_3$. Herein, peaks at $450\text{--}500\text{ }^\circ\text{C}$ correspond to the desorption of chemisorbed CO_2 .⁹ With the increase of Ce/La ratios, the desorption temperature of chemisorbed CO_2 increases to higher temperature. It indicates that Ce addition can strengthen the chemisorption of CO_2 on the surface of lanthanum species, while peaks at around $700\text{ }^\circ\text{C}$ correspond to the decomposition of $\text{II-La}_2\text{O}_2\text{CO}_3$,⁶² since the phase transformation of $\text{Ia-La}_2\text{O}_2\text{CO}_3$ to



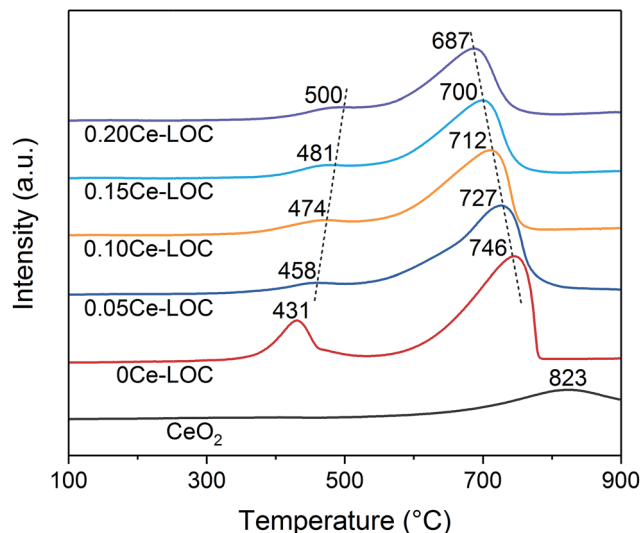


Fig. 7 H_2 -TPR profiles of the series of Ce–La binary oxides.

$\text{II-La}_2\text{O}_2\text{CO}_3$ is complete at around 600 °C.¹² With the increase of Ce/La ratios, the decomposition temperature of $\text{II-La}_2\text{O}_2\text{CO}_3$ under the H_2 atmosphere decreases to a lower temperature, indicating that Ce addition can promote the decomposition of $\text{II-La}_2\text{O}_2\text{CO}_3$ under the H_2 atmosphere, which is related to the activity in the reaction of $\text{II-La}_2\text{O}_2\text{CO}_3$ and coke.

In order to examine the performance of coke elimination, DRM reaction is used as a probe reaction, and then Ni particles are supported on the series of Ce–La binary oxide to produce coke. Ni loadings are fixed at 5 wt% for the series of Ce–La binary oxide to ensure that all catalysts exhibit similar CH_4 conversions under appropriate reaction conditions.

CO_2 -TPD was employed to investigate the basicity of the Ni supported samples (Fig. 8). It has been extensively reported that the basicity of the support is beneficial to coke elimination.⁶³

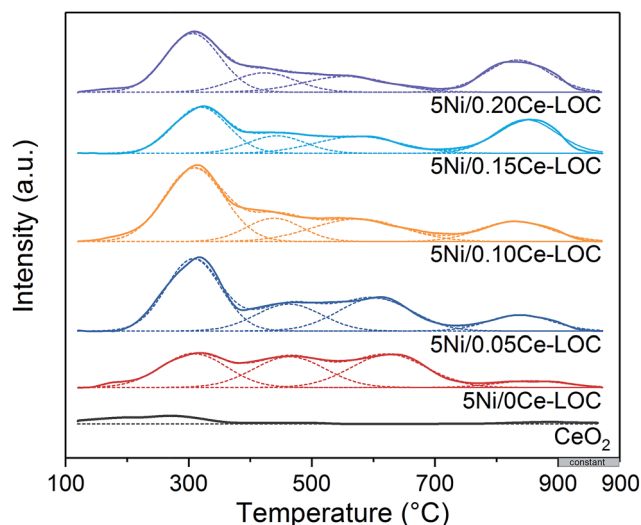


Fig. 8 CO_2 -TPD profiles of the series of Ni supported Ce–La binary oxides.

CO_2 desorption will take place when the reaction temperature (600–650 °C) is higher than the desorption temperature. Thus, basicity with higher desorption temperature should be investigated. CO_2 -TPD profiles show that areas of peaks higher than 700 °C increase with the increment of Ce/La ratio, and reach the maximum when the Ce/La ratio is 0.15, and then decrease slightly when the Ce/La ratio is 0.20. For pure CeO_2 as a reference, the area of the peak higher than 700 °C is negligible, which indicates that pure CeO_2 itself has much weaker CO_2 adsorption compared with Ce–La binary oxide. According to the DRIFTS spectra (Fig. 4, 5 and S3 in the ESI†), for the 0.15Ce-LOC sample, it has the highest intensity of bidentate carbonate during the CH_4 adsorption. A previous study by Valange *et al.* has shown that bidentate carbonate has higher stability and hence higher basicity compared with monodentate carbonate.⁶⁴ In addition, it has been reported that the decomposition temperature of $\text{II-La}_2\text{O}_2\text{CO}_3$ is higher than 700 °C.¹³ Therefore, the desorption peaks higher than 700 °C can be ascribed to the decomposition of $\text{II-La}_2\text{O}_2\text{CO}_3$. It should be mentioned that the atmosphere could affect the decomposition of $\text{La}_2\text{O}_2\text{CO}_3$,¹³ hence there is a difference in the decomposition temperature of $\text{II-La}_2\text{O}_2\text{CO}_3$ between CO_2 -TPD and H_2 -TPR (Fig. 7 and 8). For the 0.15Ce-LOC sample, it has the highest amount of bidentate carbonate after CO_2 adsorption and the highest basicity above 700 °C. It indicates that bidentate carbonate has a close relationship with $\text{II-La}_2\text{O}_2\text{CO}_3$. Based on these facts, it is assumed that Ce addition can promote the transformation from monodentate carbonate to bidentate carbonate on La_2O_3 after CO_2 adsorption, which will promote the formation of $\text{II-La}_2\text{O}_2\text{CO}_3$. On the other hand, H_2 -TPR (Fig. 7) profiles show that Ce addition improves the activity of $\text{II-La}_2\text{O}_2\text{CO}_3$ under the H_2 atmosphere.

DRM activity tests are applied to test the coke elimination performance of Ce–La binary oxide. GHSV has been adjusted to 60 000 $\text{mL h}^{-1} \text{g}_{\text{cat}}^{-1}$ to ensure that different catalysts exhibit similar CH_4 conversions. Spivey *et al.* reported that when the DRM reaction temperature is 550–650 °C, the variation

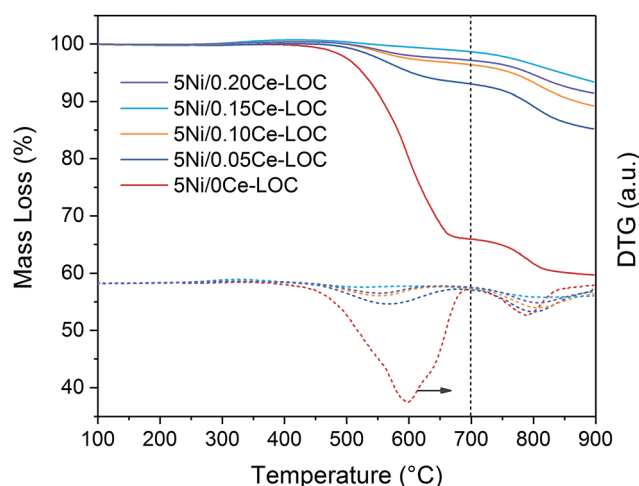


Fig. 9 TGA and DTG profiles for the spent catalysts (GHSV = 60 000 $\text{mL h}^{-1} \text{g}_{\text{cat}}^{-1}$, 650 °C, time on stream: 50 h).

tendency of coke formation is much more severe since coke originates from both CH_4 decomposition and Boudouard reaction.⁶⁵ Therefore, the reaction temperature is fixed to 650 °C to increase the coke formation. As shown in Fig. S5 in the ESI,[†] all the Ni catalysts have CH_4 conversions at around 44% and exhibit good stability.

TGA profiles are shown in Fig. 9. The mass loss below 700 °C is ascribed to the oxidation of coke and Ni particles. And the mass loss above 700 °C is ascribed to the decomposition of $\text{La}_2\text{O}_2\text{CO}_3$ to release CO_2 . At the end of TGA, all samples can be regarded as mixtures of NiO , La_2O_3 and CeO_2 . According to the Ni loading, specific Ce/La ratio and mass loss obtained by TGA, the content of Ni, CeO_2 , $\text{La}_2\text{O}_2\text{CO}_3$ and La_2O_3 in the spent catalysts can be estimated (Table 2). It should be mentioned that the formation of La_2O_3 on the spent catalysts is due to the spontaneous reaction between $\text{II-La}_2\text{O}_2\text{CO}_3$ and deposited coke. Additionally, since $\text{Ia-La}_2\text{O}_2\text{CO}_3$ is inactive for coke elimination and spontaneously transforms to $\text{II-La}_2\text{O}_2\text{CO}_3$ when the temperature is above 600 °C,^{12,16} the calculated content of $\text{La}_2\text{O}_2\text{CO}_3$ (Table 2) is ascribed to the content of $\text{Ia-La}_2\text{O}_2\text{CO}_3$ which transforms to $\text{II-La}_2\text{O}_2\text{CO}_3$ during the programmed temperature process. Therefore, we can use the calculated content of La_2O_3 and $\text{La}_2\text{O}_2\text{CO}_3$ in Table 2 to estimate the content of $\text{II-La}_2\text{O}_2\text{CO}_3$ and $\text{Ia-La}_2\text{O}_2\text{CO}_3$, respectively. Based on the results of DRIFTS (Fig. 4, 5 and S3 in the ESI[†]), bidentate carbonate is active for coke elimination while monodentate carbonate is inactive for coke elimination. When correlating the molar ratio of $\text{La}_2\text{O}_3/\text{La}_2\text{O}_2\text{CO}_3$ in Table 2 with the maximum intensity ratio of bidentate/monodentate carbonate peaks in Fig. 5, a linear relationship is obtained as shown in Fig. 10, which indicates that bidentate carbonate has a close relationship with $\text{II-La}_2\text{O}_2\text{CO}_3$ while monodentate carbonate is closely related to $\text{Ia-La}_2\text{O}_2\text{CO}_3$.

In addition, it can be found that the amount of coke decreases with the increase of Ce/La ratio. For 5Ni/0.15Ce-LOC, it has the lowest amount of coke and the highest molar ratio of $\text{La}_2\text{O}_3/\text{La}_2\text{O}_2\text{CO}_3$ after 50 h DRM reaction, indicating that appropriate Ce addition can promote the formation of $\text{II-La}_2\text{O}_2\text{CO}_3$ to react with the deposited coke. According to the DTG profiles in Fig. 9, the peak temperature of filamentous coke (~550 °C) decreases with the increase of Ce/La ratio which reflects the decrease of the graphitic degree of coke,⁴ while the peak temperature of $\text{II-La}_2\text{O}_2\text{CO}_3$ (>700 °C) exhibits the opposite variation tendency. Based on the above facts, it is concluded that the 0.15Ce-LOC sample shows the best performance for coke elimination.

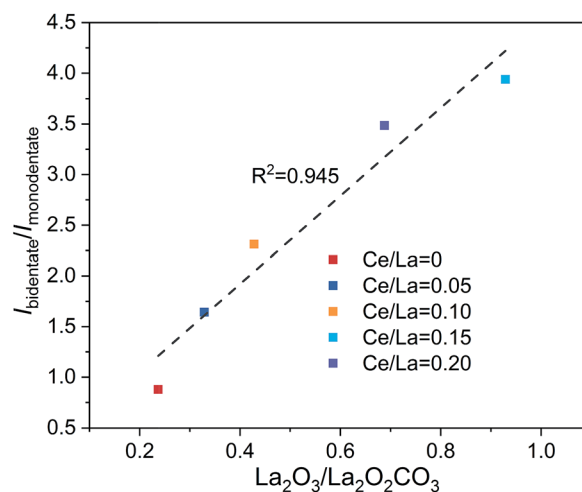


Fig. 10 Linear correlation between the molar ratio of $\text{La}_2\text{O}_3/\text{La}_2\text{O}_2\text{CO}_3$ obtained by TGA profiles and intensity ratio of bidentate/monodentate carbonate obtained by DRIFTS.

DFT calculation of CO_2 adsorption energy

DFT calculation was applied to illustrate the influence of Ce addition on the most stable CO_2 adsorption mode on $\text{La}_2\text{O}_2\text{CO}_3$ (Fig. 11). Ideally, models presuming that Ce atoms distribute along the surface layer were taken into consideration. In this case, a new C–O bond is formed between a CO_2 molecule with a surface O atom on $\text{La}_2\text{O}_2\text{CO}_3$, which leads to the formation of carbonate. The calculated frequency of the formed C–O bond is 1517 cm^{-1} , which is close to the characteristic frequency of bidentate carbonate (1560 cm^{-1}) collected by *in situ* DRIFTS (Fig. 4). In addition, the calculated CO_2 adsorption energy for pure $\text{II-La}_2\text{O}_2\text{CO}_3$ ($(\text{Ce/La})_s$ is equal to 0, the subscript s denotes surface) is -1.39 eV , which is a negative value since it is an exothermic adsorption process.

When the ratio of $(\text{Ce/La})_s$ is equal to 1 : 7, there are eight possible sites for a Ce atom to replace a La atom within our selected unit cell (Fig. S6 in the ESI[†]). DFT calculations predict that the most stable CO_2 adsorption mode takes place when the La atom at site 4 (see the definition in Fig. 11) is replaced by a Ce atom and the calculated CO_2 adsorption energy is -1.50 eV . For samples with higher Ce content, the selected model was based on the most stable structure of samples with lower Ce contents. For example, when the ratio of $(\text{Ce/La})_s$ is equal to 1 : 3, one Ce atom is fixed at the fourth site on the basis of the obtained

Table 2 Quantitative analysis of TGA profiles

Sample	Mass loss (%)		Component in the spent catalysts (%)					Molar ratio of $\text{La}_2\text{O}_3/\text{La}_2\text{O}_2\text{CO}_3$	Amount of coke ($\text{g g}_{\text{cat}}^{-1}$)	Rate of coke formation ($\mu\text{mol g}_{\text{cat}}^{-1}\cdot\text{s}^{-1}$)
	<700 °C	>700 °C	Coke	Ni	CeO_2	$\text{La}_2\text{O}_2\text{CO}_3$	La_2O_3			
5Ni/0Ce-LOC	33.9	6.2	33.9	3.1	0	52.1	10.9	0.237	0.513	0.237
5Ni/0.05Ce-LOC	6.9	7.8	6.9	4.4	4.2	65.5	19.0	0.329	0.074	0.034
5Ni/0.10Ce-LOC	3.9	7.2	3.9	4.5	8.2	60.5	22.8	0.428	0.041	0.019
5Ni/0.15Ce-LOC	2.2	5.3	2.2	4.7	12.1	44.5	36.5	0.929	0.022	0.010
5Ni/0.20Ce-LOC	3.2	5.7	3.2	4.6	15.3	47.9	29.0	0.688	0.033	0.015



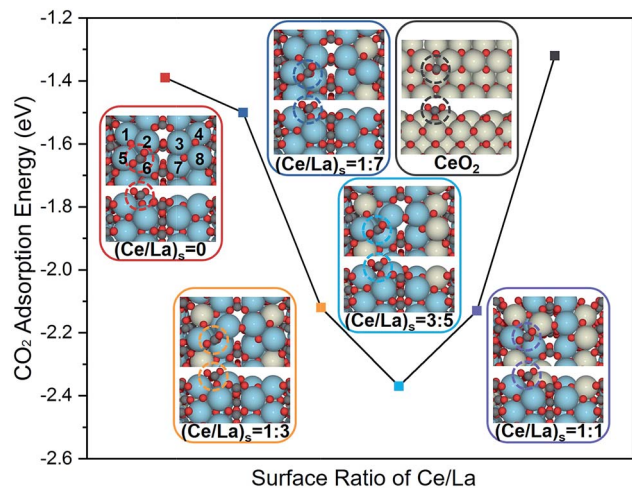


Fig. 11 Calculated CO₂ adsorption energies on the surfaces of Ce–La binary oxides and corresponding top and side views of geometries with CO₂ adsorbed on the top site of binary oxides. Colors: yellow, Ce; blue, La; grey, C; and red, O.

calculation (Fig. S7 in the ESI†). In this case, the most stable CO₂ adsorption mode takes place when La atoms located at sites 1 and 4 are replaced by Ce atoms and the calculated adsorption energy is -2.12 eV. Following the same procedure, when the ratio of (Ce/La)_s increases to 3 : 5 and 1 : 1, the strongest adsorption energy of CO₂ over Ce–La binary oxides is -2.37 eV (Fig. S8 in the ESI†) and -2.13 eV (Fig. S9 in the ESI†), respectively. Meanwhile, twenty extra models with randomly distributed Ce structures were tested, which did not follow the mentioned procedure. The CO₂ binding over all these randomly generated models is less stable than the ones discussed above (Table S1 in the ESI†). Additionally, the calculated CO₂ adsorption energy for pure CeO₂ is -1.32 eV, which is weaker than that of La₂O₂CO₃ and other Ce–La binary oxides. It indicates that the intensity of CO₂ adsorption on ceria is much weaker than that of La₂O₂CO₃ and other Ce–La binary oxides, which is responsible for the absence of bidentate carbonate on CeO₂ as shown in Fig. 4.

According to the results of DFT calculation (Fig. 11), with the increase of (Ce/La)_s ratios, the CO₂ adsorption energy gradually becomes lower and reaches the lowest value when (Ce/La)_s is equal to 3 : 5, and then the CO₂ adsorption energy weakens. The variation tendency of CO₂ adsorption energy with the increase of (Ce/La)_s ratios (Fig. 11) is consistent with the variation tendency for the peak intensity of bidentate carbonate on Ce–La binary oxides (Fig. 4). As the CO₂ adsorption energy becomes lower, CO₂ adsorption on binary oxide is strengthened, and the formed carbonate is expected to have better stability. Therefore, Ce addition can affect CO₂ adsorption energy for Ce–La binary oxide and the type of carbonate formed after CO₂ adsorption. Ce–La binary oxide with the optimal Ce/La ratio exhibits the highest intensity of bidentate carbonate (Fig. 4), and hence has the highest basicity above 700 °C (Fig. 8) and shows the best coke elimination performance (Fig. 9).

Conclusion

We have investigated the role of Ce addition in CO₂ adsorption and activation over lanthanum species. Based on results of *in situ* DRIFTS spectra, DFT calculations and other experimental characterizations, it is concluded that Ce addition can promote the formation of bidentate carbonate on Ce–La binary oxide *via* tuning CO₂ adsorption energy. With the increase of Ce/La ratio from 0 to 0.20, Ce addition facilitates transformation from monodentate carbonate to bidentate carbonate on Ce–La binary oxides. Bidentate carbonate is verified to be active in the reaction with deposited coke, while monodentate carbonate is inactive for coke elimination. With the consumption of bidentate carbonate, the variation of the intensity ratio of bidentate/monodentate carbonate can affect the ratio of II-La₂O₂CO₃/Ia-La₂O₂CO₃. Bidentate carbonate is verified to be closely related to II-La₂O₂CO₃ and monodentate carbonate has a close relationship with Ia-La₂O₂CO₃. When the Ce/La ratio is 0.15, the corresponding nickel catalyst has the highest intensity ratio of bidentate/monodentate carbonate and the highest ratio of II-La₂O₂CO₃/Ia-La₂O₂CO₃, which exhibits the highest basicity above 700 °C and the best performance of coke elimination after 50 h DRM reaction.

Experimental section

Catalyst preparation

Analytical grade La(NO₃)₃·6H₂O, Ce(NO₃)₃·6H₂O, Ni(NO₃)₂·6H₂O and CeO₂ powder were obtained from Aladdin Industrial Corporation (Shanghai, China). Analytical grade aqueous ammonia (25 wt%) and anhydrous ethanol (99.8 wt%) were obtained from Guangfu Fine Chemical Research Institute (Tianjin, China). Guaranteed grade urea was supplied by Kermel Chemical Reagent (Tianjin, China). De-ionized water (18.0 MΩ) was prepared using an Ulupure water purifier machine (Chengdu, China).

The synthesis route of La₂O₂CO₃ is described as follows. 2.6 grams of La(NO₃)₃·6H₂O and 7.2 grams of urea were separately dissolved in de-ionized water. Once dissolved, the two solutions were mixed with constant stirring; the concentrations of La³⁺ and urea in the mixture were 0.015 mol L⁻¹ and 0.30 mol L⁻¹, respectively. Then aqueous ammonia was added into the mixture to adjust the pH to 8.5. A white suspension was obtained after heating in a water bath at 90 °C for 3 h with constant stirring, followed by naturally cooling to room temperature. Afterwards, the white suspension was centrifuged and washed with absolute ethanol three times. La₂O₂CO₃ was finally prepared upon drying at 80 °C overnight and calcination at 500 °C for 2 h.

A series of Ce–La binary oxides were prepared by a wet impregnation method. The stoichiometric Ce/La ratio was chosen as 0, 0.05, 0.10, 0.15, and 0.20, respectively. The prepared La₂O₂CO₃ was impregnated with an aqueous solution containing a specified amount of Ce(NO₃)₂·6H₂O. Upon stirring at 80 °C for 3 h, vacuum evaporation was carried out to remove the solvent. Then the sample was dried overnight, and ground and calcined at 600 °C for 2 h. The prepared Ce–La binary oxide



was marked as “ $x\text{Ce-LOC}$ ”, where LOC denotes the prepared $\text{La}_2\text{O}_2\text{CO}_3$ and x denotes the specific stoichiometric Ce/La ratio.

A series of Ni catalysts supported on the prepared Ce–La binary oxide were synthesized by a similar procedure to that described above. For the subsequent wet impregnation method the Ni loading was fixed at 5 wt% on the basis of reduction conditions. When the sample was impregnated with the Ni precursor and dried overnight, it was ground and calcined at 650 °C for 2 h. After grinding to 20–40 mesh, the sample was reduced at 650 °C under a H_2 atmosphere ($\text{H}_2/\text{N}_2 = 1 : 3$, 40 mL min^{-1}) for 60 min. The prepared catalyst was named 5Ni/ $x\text{Ce-LOC}$, where LOC denotes the prepared $\text{La}_2\text{O}_2\text{CO}_3$ and x denotes the specific Ce/La ratio.

Characterization

Textural properties of catalysts were measured through nitrogen adsorption–desorption at -196°C using a Micromeritics Tristar 3000 analyzer. All samples were degassed at 300 °C for 3 h prior to the tests. The specific surface areas were calculated on the basis of the N_2 isotherms and the Brunauer–Emmett–Teller (BET) method. Combined with the Barrett–Joyner–Halenda (BJH) method and the desorption branches of the N_2 isotherms, cumulative volumes of pores were obtained.

Elemental contents of the prepared catalysts were examined by inductively coupled plasma optical emission spectroscopy (ICP-OES) (VISTA-MPX, Varian) at a high frequency emission power of 1.5 kW and a plasma airflow of 15.0 L min^{-1} ($\lambda_{\text{Ni}} = 231.60 \text{ nm}$, $\lambda_{\text{La}} = 379.48 \text{ nm}$, $\lambda_{\text{Ce}} = 413.76 \text{ nm}$). Prior to measurements, samples were dissolved in a mixture of nitric acid and H_2O_2 to ensure that the concentrations of the measured elements are close to the concentrations of the prepared standard solutions.

XRD patterns were examined through a Rigaku D/max-2500 diffractometer equipped with graphite filtered Cu $K\alpha$ radiation ($\lambda = 1.54056 \text{ \AA}$), and 2θ values range from 20° to 80° . The mean crystalline size of Ni particles was calculated by Scherrer's equation according to the diffraction peaks of Ni (111) facets.

H_2 -TPR experiment was applied to analyze the reduction behavior of the catalysts with the aid of a chemisorption apparatus (Micromeritics AutoChem II 2920). 100 mg of the sample was pretreated at 300 °C for 1 h with an Ar stream (30 mL min^{-1}) to remove moisture and impurities. After cooling to 50 °C, the system was exposed to a 10 vol% H_2/Ar stream (30 mL min^{-1}) to reduce the sample. Subsequently, the temperature of the system was programmed to rise linearly from 100 °C to 900 °C with a rate of $10^\circ\text{C min}^{-1}$, during which variation of the signal of the thermal conductivity detector (TCD) was recorded.

CO_2 -TPD analysis was applied to investigate the basicity of the catalyst by utilizing the same chemisorption apparatus (Micromeritics AutoChem II 2920). 100 mg of the sample was prereduced at 750 °C with a 10 vol% H_2/Ar stream (50 mL min^{-1}) for 30 min to completely decompose existing $\text{La}_2\text{O}_2\text{CO}_3$ on samples before CO_2 adsorption. After cooling to 60 °C, the system was exposed to a stream of CO_2 gas (50 mL min^{-1}) to carry out CO_2 adsorption for 30 min. Next, the

system was exposed to a He stream (30 mL min^{-1}) and the temperature was programmed to increase to 120 °C for the removal of residual CO_2 in the stream. Once the signal of TCD reached a stable state, the temperature of the system was programmed to increase from 120 °C to 900 °C with a ramping rate of $10^\circ\text{C min}^{-1}$ and at the same time the system starts to keep record of the TCD signal. An isothermal period lasting for 8 minutes at 900 °C was set to ensure that the adsorbed CO_2 was totally desorbed.

A TEM instrument (FEI Tecnai G2 F20) was applied to investigate the morphology and structure of catalysts, and the working voltage was 100 kV. After the sample powder was dispersed in absolute ethanol *via* ultrasonication, the obtained suspension was dripped onto a copper grid-supported transparent carbon foil and dried in air for characterization.

XPS analysis of the catalysts was carried out on a Perkin-Elmer PHI 1600 ESCA system equipped with an Al KR X-ray source ($E = 1486.6 \text{ eV}$). Spectra were operated at a pass energy of 187.85 eV. The binding energy (B.E.) scale was measured on the basis of carbon contamination utilizing C 1s peak centered at 285 eV. In addition, core peaks were obtained using a nonlinear Shirley-type background. Besides, quantification of surface elemental composition was carried out according to Scofield's relative sensitivity factors.⁶⁶

Properties of the coke deposited on the spent catalysts were characterized by utilizing a TGA system (STA449F3, NETZSCH Corp.). The TGA experiment was conducted in an air stream (50 mL min^{-1}), and the temperature was programmed to rise from room temperature to 900 °C with a heating rate of $10^\circ\text{C min}^{-1}$. The amount of coke deposition, $\text{II-La}_2\text{O}_2\text{CO}_3$ accumulation and oxidation of Ni particles were calculated according to the mass losses in TGA profiles.

A Raman spectrometer (Renishaw inVia Reex) was employed to record Raman spectra under ambient conditions, which was equipped with a 532 nm Ar-ion laser beam as the excitation source. Each sample was examined more than three times at different positions.

UV-visible reflectance spectra were collected on a SHIMADZU UV-2550 spectrophotometer using a pressed disc of the sample. Kubelka–Munk transformed diffuse reflectance spectra (DRS) of all samples were measured with BaSO_4 powder as a reference.

In situ DRIFTS measurements

In situ DRIFTS experiments were performed on a ThermoFisher Nicolet IS50 spectrometer, which was equipped with a Harrick Scientific diffuse reflection accessory and a mercury–cadmium–telluride (MCT) detector. The scheme of the experimental process is shown in Fig. 1. The Ce–La binary oxide samples were placed in the cell of the DRIFTS apparatus and reduced at 600 °C under 30 vol% H_2/Ar stream (30 mL min^{-1}). And then, the gas stream was switched from H_2/Ar stream to Ar stream (30 mL min^{-1}) in order to remove hydrogen in the gas stream. Subsequently, the baseline of DRIFTS was collected continuously until the obtained baseline spectra remained stable. Afterwards, the gas stream was switched to 10 vol% CO_2/Ar stream (30 mL min^{-1}) to carry out CO_2 adsorption for 30 min,



after which the CO₂ adsorption was saturated. The moment at the end of CO₂ adsorption was marked as “0 min”. Subsequently, the gas stream was switched from 10 vol% CO₂/Ar stream to 10 vol% CH₄/Ar stream (30 mL min⁻¹) in order to carry out CH₄ adsorption for 30 min. The moment at the end of CH₄ adsorption was marked as “30 min”. *In situ* DRIFTS measurements were carried out from “0 min” to “30 min”. Since DRIFTS spectra remained stable after “30 min”, it could be regarded that the reaction took place completely. Additionally, when it is “0 min” or “30 min”, subsequent operations could be skipped and the temperature would decrease from 600 °C to room temperature. When the cell was cooled to room temperature, samples could be taken out to carry out *ex situ* characterizations.

Periodic DFT calculations

Periodic DFT calculations were carried out with the assistance of Vienna *ab initio* Simulation Package (VASP).⁶⁷ The calculations employed the generalized-gradient approximation (GGA) in the form of the Perdew–Burke–Ernzerhof (PBE) exchange–correlation functional.⁶⁸ A Hubbard U value was added to the PBE functional (DFT + U), which is chosen to improve the quality of the DFT calculations in dealing with oxides having narrow f or d bands.⁶⁹ The interactions between the atomic cores and electrons were described by the projector augmented wave (PAW) method.⁷⁰ The valence wave functions were expanded using plane-wave with a cutoff energy of 400 eV. A 4 × 2 cell was used for La₂O₂CO₃ (110) and CeO₂ (110) surfaces, and a 3 × 1 × 1 *k*-point mesh was used for the Brillouin zone integration. The slab was three layers thick and separated by 15 Å of vacuum. The top two layers of the slab were allowed to relax, while the bottom one layer was kept fixed. For La, a value of $U_{\text{eff}} = 7.5$ eV was used, which was calculated self-consistently by Metiu *et al.*¹⁹ $U_{\text{eff}} = 4.5$ eV was employed for Ce, which was reported by Fabris *et al.*⁷¹

The adsorption energy of adsorbates, E_{ads} , is defined as follows:

$$E_{\text{ads}} = E_{\text{total}} - E_{\text{gas}} - E_{\text{slab}}, \quad (2)$$

where E_{total} is the total energy of the system after adsorption, E_{gas} is the energy of the adsorbate in the gas phase, and E_{slab} is the energy of the clean slab. Thus, a negative value means an exothermic adsorption process.

Coke elimination performance test

Catalytic activity tests were carried out in a quartz fixed-bed tubular reactor (Φ 8 × 44 mm) under atmospheric pressure. Prior to the test, the catalyst sample (100 mg, 20–40 mesh) was evenly mixed with 1 mL of quartz particles and then the mixture was loaded inside the reactor. Prior to the test, the catalysts were reduced at 650 °C under a 25 vol% H₂/N₂ stream (40 mL min⁻¹) for an hour. The flow rate of the feed gas was set at 100 mL min⁻¹ (GHSV = 60 000 mL h⁻¹ g_{cat}⁻¹, CH₄ : CO₂ : N₂ = 20 : 20 : 60 mL min⁻¹) to ensure that the activities of the catalysts are close to each other to simplify the comparison of coke

deposition. Here, the mentioned GHSV is based on a total flow. The concentrations of gas species including CH₄, CO₂, H₂, CO, and N₂ were measured online with the assistance of a gas chromatograph (GC2060, Shanghai Ruimin Instrument). Helium was used as the carrier gas. The GC was equipped with a TCD and two columns including a TDX-01 column followed by a 5 Å molecular sieve column. Activity test was performed at 650 °C for 50 h. Conversions of CH₄ and CO₂ (X_{CH_4} and X_{CO_2}), selectivities to H₂ and CO (S_{H_2} and S_{CO}), and the H₂/CO ratio are defined as follows:

$$X_{\text{CH}_4} = \frac{F_{\text{CH}_4,\text{in}} - F_{\text{CH}_4,\text{out}}}{F_{\text{CH}_4,\text{in}}} \quad (3)$$

$$X_{\text{CO}_2} = \frac{F_{\text{CO}_2,\text{in}} - F_{\text{CO}_2,\text{out}}}{F_{\text{CO}_2,\text{in}}} \quad (4)$$

$$S_{\text{H}_2} = \frac{F_{\text{H}_2,\text{out}}}{2 \times (F_{\text{CH}_4,\text{in}} - F_{\text{CH}_4,\text{out}})} \quad (5)$$

$$S_{\text{CO}} = \frac{F_{\text{CO},\text{out}}}{(F_{\text{CH}_4,\text{in}} - F_{\text{CH}_4,\text{out}}) + (F_{\text{CO}_2,\text{in}} - F_{\text{CO}_2,\text{out}})} \quad (6)$$

$$\text{H}_2/\text{CO} = \frac{F_{\text{H}_2,\text{out}}}{F_{\text{CO},\text{out}}} \quad (7)$$

Conflicts of interest

There are no conflicts to declare.

Acknowledgements

We thank the National Key R&D Program of China (2016YFB0600901), the National Natural Science Foundation of China (No. 51761145012, 21525626, and U1663224) and the Program of Introducing Talents of Discipline to Universities (No. B06006) for financial support.

References

- 1 C. Montero, A. Ochoa, P. Castaño, J. Bilbao and A. G. Gayubo, *J. Catal.*, 2015, **331**, 181–192.
- 2 S. Singh, D. Zubenko and B. A. Rosen, *ACS Catal.*, 2016, **6**, 4199–4205.
- 3 H. Chen, H. Yu, F. Peng, H. Wang, J. Yang and M. Pan, *J. Catal.*, 2010, **269**, 281–290.
- 4 X. Li, D. Li, H. Tian, L. Zeng, Z.-J. Zhao and J. Gong, *Appl. Catal., B*, 2017, **202**, 683–694.
- 5 X. E. Verykios, *Int. J. Hydrogen Energy*, 2003, **28**, 1045–1063.
- 6 Z. Zhang, X. E. Verykios, S. M. MacDonald and S. Affrossman, *J. Phys. Chem.*, 1996, **100**, 744–754.
- 7 Z. Zhang and X. E. Verykios, *Appl. Catal., A*, 1996, **138**, 109–133.
- 8 V. A. Tsipouriari and X. E. Verykios, *Catal. Today*, 2001, **64**, 83–90.



- 9 Y. H. Hou, W. C. Han, W. S. Xia and H. L. Wan, *ACS Catal.*, 2015, **5**, 1663–1674.
- 10 R. P. Taylor and G. L. Schrader, *Ind. Eng. Chem. Res.*, 1991, **30**, 1016–1023.
- 11 R. P. Turcotte, J. O. Sawyer and L. Eyring, *Inorg. Chem.*, 1969, **8**, 238–246.
- 12 A. Orera, G. Larraz and M. L. Sanjuán, *J. Eur. Ceram. Soc.*, 2013, **33**, 2103–2110.
- 13 S. Irusta, L. M. Cornaglia and E. A. Lombardo, *Mater. Chem. Phys.*, 2004, **86**, 440–447.
- 14 T. Levan, M. Che, J. M. Tatibouet and M. Kermarec, *J. Catal.*, 1993, **142**, 18–26.
- 15 B. Klingenberg and M. A. Vannice, *Chem. Mater.*, 1996, **8**, 2755–2768.
- 16 D. Pakhare, V. Schwartz, V. Abdelsayed, D. Haynes, D. Shekhawat, J. Poston and J. Spivey, *J. Catal.*, 2014, **316**, 78–92.
- 17 G. Yang, H. Yu, X. Huang, F. Peng and H. Wang, *Appl. Catal., B*, 2012, **127**, 89–98.
- 18 L. Jin, Y. Zhang, J. P. Dombrowski, C.-H. Chen, A. Pravatas, L. Xu, C. Perkins and S. L. Suib, *Appl. Catal., B*, 2011, **103**, 200–205.
- 19 B. Li and H. Metiu, *J. Phys. Chem. C*, 2010, **114**, 12234–12244.
- 20 B. Li and H. Metiu, *J. Phys. Chem. C*, 2011, **115**, 18239–18246.
- 21 T. Montini, M. Melchionna, M. Monai and P. Fornasiero, *Chem. Rev.*, 2016, **116**, 5987–6041.
- 22 J. A. Rodriguez, D. C. Grinter, Z. Liu, R. M. Palomino and S. D. Senanayake, *Chem. Soc. Rev.*, 2017, **46**, 1824–1841.
- 23 S. Bhavsar, N. Isenberg, A. More and G. Veser, *Appl. Energy*, 2016, **168**, 236–247.
- 24 W. Xu, Z. Liu, A. C. Johnston-Peck, S. D. Senanayake, G. Zhou, D. Stacchiola, E. A. Stach and J. A. Rodriguez, *ACS Catal.*, 2013, **3**, 975–984.
- 25 D. Li, X. Li and J. Gong, *Chem. Rev.*, 2016, **116**, 11529–11653.
- 26 S. Li and J. Gong, *Chem. Soc. Rev.*, 2014, **43**, 7245–7256.
- 27 E. T. Saw, U. Oemar, X. R. Tan, Y. Du, A. Borgna, K. Hidajat and S. Kawi, *J. Catal.*, 2014, **314**, 32–46.
- 28 S. Chen, L. Luo, Z. Jiang and W. Huang, *ACS Catal.*, 2015, **5**, 1653–1662.
- 29 H. Muroyama, S. Hano, T. Matsui and K. Eguchi, *Catal. Today*, 2010, **153**, 133–135.
- 30 H. Muroyama, H. Asajima, S. Hano, T. Matsui and K. Eguchi, *Appl. Catal., A*, 2015, **489**, 235–240.
- 31 J. Li, X. Liu, W. Zhan, Y. Guo, Y. Guo and G. Lu, *Catal. Sci. Technol.*, 2016, **6**, 897–907.
- 32 M. Zhao, M. Shen and J. Wang, *J. Catal.*, 2007, **248**, 258–267.
- 33 J.-R. Kim, W.-J. Myeong and S.-K. Ihm, *Appl. Catal., B*, 2007, **71**, 57–63.
- 34 L. Katta, P. Sudarsanam, G. Thrimurthulu and B. M. Reddy, *Appl. Catal., B*, 2010, **101**, 101–108.
- 35 B. Zhang, D. Li and X. Wang, *Catal. Today*, 2010, **158**, 348–353.
- 36 K. Harada, T. Oishi, S. Hamamoto and T. Ishihara, *J. Phys. Chem. C*, 2014, **118**, 559–568.
- 37 B. M. Reddy, L. Katta and G. Thrimurthulu, *Chem. Mater.*, 2010, **22**, 467–475.
- 38 A. Bueno-López, K. Krishna, M. Makkee and J. A. Moulijn, *J. Catal.*, 2005, **230**, 237–248.
- 39 Z. Stansch, L. Mleczko and M. Baerns, *Ind. Eng. Chem. Res.*, 1997, **36**, 2568–2579.
- 40 M. Taniewski, A. Lachowicz, R. Lachowicz, D. Czechowicz and K. Skutil, *Ind. Eng. Chem. Res.*, 1994, **33**, 185–190.
- 41 D. Pakhare and J. Spivey, *Chem. Soc. Rev.*, 2014, **43**, 7813–7837.
- 42 S. Damyanova, B. Pawelec, K. Arishtirova, M. V. M. Huerta and J. L. G. Fierro, *Appl. Catal., A*, 2008, **337**, 86–96.
- 43 F. ç. Larachi, J. Pierre, A. Adnot and A. Bernis, *Appl. Surf. Sci.*, 2002, **195**, 236–250.
- 44 R. Leppelt, B. Schumacher, V. Plzak, M. Kinne and R. J. Behm, *J. Catal.*, 2006, **244**, 137–152.
- 45 A. Karpenko, Y. Denkwitz, V. Plzak, J. Cai, R. Leppelt, B. Schumacher and R. J. Behm, *Catal. Lett.*, 2007, **116**, 105–115.
- 46 C. Yang, X. Yu, S. Heißler, A. Nefedov, S. Colussi, J. Llorca, A. Trovarelli, Y. Wang and C. Wöll, *Angew. Chem., Int. Ed.*, 2017, **56**, 375–379.
- 47 S. Deshpande, S. Patil, S. V. Kuchibhatla and S. Seal, *Appl. Phys. Lett.*, 2005, **87**, 133113.
- 48 C. A. Orge, J. J. M. Órfão, M. F. R. Pereira, A. M. Duarte de Farias, R. C. R. Neto and M. A. Fraga, *Appl. Catal., B*, 2011, **103**, 190–199.
- 49 C. Ho, J. C. Yu, T. Kwong, A. C. Mak and S. Lai, *Chem. Mater.*, 2005, **17**, 4514–4522.
- 50 B. Liu, Q. Li, X. Du, B. Liu, M. Yao, Z. Li, R. Liu, D. Liu, X. Zou, H. Lv, D. Li, B. Zou, T. Cui and G. Zou, *J. Alloys Compd.*, 2011, **509**, 6720–6724.
- 51 M. Sorescu, T. Xu, J. D. Burnett and J. A. Aitken, *J. Mater. Sci.*, 2011, **46**, 6709–6717.
- 52 E. M. Wilcox, G. W. Roberts and J. J. Spivey, *Catal. Today*, 2003, **88**, 83–90.
- 53 B. Bachiller-Baeza, C. Mateos-Pedrero, M. A. Soria, A. Guerrero-Ruiz, U. Rodemerck and I. Rodríguez-Ramos, *Appl. Catal., B*, 2013, **129**, 450–459.
- 54 S. J. Huang, A. B. Walters and M. A. Vannice, *Appl. Catal., B*, 2000, **26**, 101–118.
- 55 M. P. Rosynek and D. T. Magnuson, *J. Catal.*, 1977, **48**, 417–421.
- 56 L. M. Cornaglia, J. Múnera, S. Irusta and E. A. Lombardo, *Appl. Catal., A*, 2004, **263**, 91–101.
- 57 B. M. Faroldi, J. F. Múnera and L. M. Cornaglia, *Appl. Catal., B*, 2014, **150–151**, 126–137.
- 58 X. B. Wang, C. Song, K. W. Geng, F. Zeng and F. Pan, *Appl. Surf. Sci.*, 2007, **253**, 6905–6909.
- 59 Z.-Y. Pu, J.-Q. Lu, M.-F. Luo and Y.-L. Xie, *J. Phys. Chem. C*, 2007, **111**, 18695–18702.
- 60 A. D. Liyanage, S. D. Perera, K. Tan, Y. Chabal and K. J. Balkus, *ACS Catal.*, 2014, **4**, 577–584.
- 61 J. Ni, L. Chen, J. Lin, M. K. Schreyer, Z. Wang and S. Kawi, *Int. J. Hydrogen Energy*, 2013, **38**, 13631–13642.
- 62 M. M. Nair, S. Kaliaguine and F. Kleitz, *ACS Catal.*, 2014, **4**, 3837–3846.
- 63 H. Ma, L. Zeng, H. Tian, D. Li, X. Wang, X. Li and J. Gong, *Appl. Catal., B*, 2016, **181**, 321–331.



- 64 S. Valange, A. Beauchaud, J. Barrault, Z. Gabelica, M. Daturi and F. Can, *J. Catal.*, 2007, **251**, 113–122.
- 65 S. Gaur, D. J. Haynes and J. J. Spivey, *Appl. Catal., A*, 2011, **403**, 142–151.
- 66 J. H. Scofield, *J. Electron Spectrosc. Relat. Phenom.*, 1976, **8**, 129–137.
- 67 G. Kresse and J. Furthmüller, *Comput. Mater. Sci.*, 1996, **6**, 15–50.
- 68 Z.-J. Zhao, A. Kulkarni, L. Vilella, J. K. Nørskov and F. Studt, *ACS Catal.*, 2016, **6**, 3760–3766.
- 69 G. Pacchioni, *J. Chem. Phys.*, 2008, **128**, 182505.
- 70 P. E. Blöchl, *Phys. Rev. B: Condens. Matter Mater. Phys.*, 1994, **50**, 17953–17979.
- 71 S. Fabris, S. de Gironcoli, S. Baroni, G. Vicario and G. Balducci, *Phys. Rev. B: Condens. Matter Mater. Phys.*, 2005, **72**, 237102.

